RSC Advances

PAPER

View Article Online
View Journal | View Issue

Cite this: *RSC Adv.*, 2025, **15**, 20589

Tuning the physical properties of SnO_2 quantum dots *via* Ag-doping for fabricating efficient photodetectors†

Rahul Sonkar, [ab] Bitopan Boro, [ab] Anand Pandey, [c] Mritunjoy Prasad Ghosh *[a] and Devasish Chowdhury *[ab]

In order to satisfy the increasing demand for affordable photodetectors in the sectors of flexible electronics and contemporary medical devices in this decade, researchers are looking for efficient semiconducting nanomaterials globally. Ag-doped SnO_2 quantum dots (QDs) with varying Ag ion concentrations were synthesized *via* chemical co-precipitation for efficient photodetector fabrication. The impact of Ag dopants on SnO_2 QDs properties was analyzed through multiple characterization techniques. X-ray diffraction and Raman spectra confirmed an impurity-free crystal structure. Crystallite sizes (2.9–3.4 nm), calculated using Scherrer's formula, were below the Bohr excitonic diameter, validating their quantum dot nature. TEM images aligned with crystallite sizes, further confirming QD formation. The observed blue shift in band gaps with increasing Ag dopants is attributed to quantum confinement due to the reduction in mean particle size. Theoretically, the estimated values of absorption cross sections and electric field intensity of SnO_2 QDs and Ag-doped SnO_2 QDs using the finite time domain method were found to be in harmony with UV-Vis spectroscopy results. The obtained FTIR spectra of all the QDs demonstrated distinct peaks corresponding to different chemical bonds, further validated the phase purity. Ag-doped SnO_2 QDs show lower PL intensity than pure SnO_2, indicating better charge separation and less recombination. Including photodetector application, the highest Ag-doped SnO_2 QD sample is expected to have more active sites and be more suitable for various applications, such as photocatalytic and antioxidant capabilities, because of its higher specific surface area. Room temperature Hall effect experiments revealed that the pure SnO_2 QDs showed the p-type semiconducting nature, whereas, with the addition of metal Ag ions, electrons became the majority charge carriers and the doped samples turned into n-type semiconductors. We have fabricated photodetectors using as-prepared samples and found that 6% Ag-doped SnO_2 QDs showed better performance when compared with the other two samples. In addition to that, the free-radical scavenging activities of all the QDs were determined and it was found that SnO_2 QDs doped with Ag ions have better antioxidant properties than pure SnO_2 QDs. Consequently, these Ag-doped SnO_2 QDs were found to be effective for photodetector application and reducing the oxidative stress.

Received 4th June 2025
Accepted 10th June 2025

DOI: 10.1039/d5ra03972j

rsc.li/rsc-advances

1. Introduction

In this decade, the advancement of optoelectronic and modern medical devices to become more flexible and highly efficient raises the need for environment-friendly, cost-effective and novel semiconducting materials. Researchers are actively searching for efficient materials worldwide to fulfill the growing demand for modern technological advancement. Photodetectors have become essential optoelectronic devices because they bridge the gap between photons and electrons by transforming light into an electrical current.[1–3] For enhancing its performance and fast response, development of novel photoactive materials is necessary. In this regard, metal oxides, doped semiconductors, quantum dots and semiconductor alloys have been thoroughly investigated as effective nanomaterials for fabricating highly efficient photodetectors for use in optical sensing, imaging systems, flexible electronics, security, and various medical applications. A lot of research has been carried out widely to explore the photodetectors applications of several semiconducting nanomaterials together with energy conversion, environmental remediation, and solar energy harvesting

[a]*Material Nanochemistry Laboratory, Physical Sciences Division, Institute of Advanced Study in Science and Technology, Paschim Boragaon, Garchuk, Guwahati-781035, Assam, India. E-mail: mritunjoyprasad92@gmail.com; devasish@iasst.gov.in*

[b]*Academy of Scientific and Innovative Research (AcSIR), Ghaziabad-201002, India*

[c]*Centre for Nanotechnology, Indian Institute of Technology Guwahati, Guwahati-781039, Assam, India*

† Electronic supplementary information (ESI) available. See DOI: https://doi.org/10.1039/d5ra03972j

applications. In the design and construction of photodetectors, nanomaterials like graphene, quantum dots, nanowires, transition metal dichalcogenides, semiconducting nanoparticles, and perovskite nanocrystals have shown great promise.[4–8] Better sensitivity, quicker reaction times, and wider spectrum detection ranges are made possible by using nanomaterials due to their high surface-to-volume ratio, configurable electronic bandgap, and enhanced charge transport characteristics. In this direction, a wide bandgap SnO_2 semiconductor in a nanoscale regime with tunable physical properties and optical bandgap may potentially be used in the direction of photodetector applications. Doping suitable ions in appropriate amounts is one of the easiest ways to modify the physical properties of a compound as per the requirements.[9–11]

SnO_2 semiconductors are typically diamagnetic in nature, with significant excitonic binding energy (130 meV) and Bohr excitonic diameter (5.4 nm). Silver (Ag) ions incorporation is one type of doping approach that has been utilized to change the bandgap and also enhance the photodetector efficiency of SnO_2 QDs. Silver may alter the electronic structure of SnO_2 and facilitate the charge carrier separation, subsequently increasing the photodetector performance.[12–16] Apart from photodetector application, the doped Ag ions in SnO_2 QDs can serve as effective electron sinks, reducing the rates of charge carrier recombination and increasing the overall efficiency of the photocatalytic process. Ag-doped SnO_2 QDs combine the advantageous characteristics of SnO_2, like good thermal, chemical stability and n-type conductivity, with enhanced optical properties and modified photoactive activities brought by silver doping.[17–19] The doping method makes SnO_2 more beneficial and opens up new applications in the photovoltaic, photodetector, sensor, and environmental cleanup industries. Charge carrier dynamics are enhanced by adding silver atoms to the SnO_2 lattice, optimizing the QDs for various technological advancements.[4–8,17–20]

Ag-doped SnO_2 quantum dots (QDs) demonstrate significant potential in various electronic applications due to their enhanced electrical, optical, and structural properties. Ag-doped SnO_2 QDs are currently being investigated for use in optoelectronic devices, such as quantum dot light-emitting diodes (QLEDs). These materials offer improved electroluminescence efficiency and operational stability, making them promising candidates for next-generation display technologies.[21] In photovoltaics, SnO_2 QDs have been utilized as electron transport layers (ETLs) in perovskite solar cells. Their high electron mobility and transparency contribute to enhanced power conversion efficiencies. Moreover, incorporating Ag doping can further improve charge transport and device stability.[22] Additionally, Ag-doped SnO_2 QDs have been explored as anode materials in lithium-ion batteries. Their high surface area and improved electrical conductivity contribute to higher capacity and better cycling stability. These properties are essential for developing high-performance energy storage systems.[23]

Different synthesis techniques that allow for precise control over the growth mechanism have been developed in recent decades to produce nanoparticles or quantum dots. The conventional wet chemical co-precipitation method is one of the most widely used bottom-up production pathways for nanoparticles and quantum dots among all these accessible synthesis techniques because it offers great control over size and shape and is also a simpler and more affordable method.[12–17] Ag-doped SnO_2 QDs have strong photoactive properties as well as the ability to neutralize and scavenge free radicals that produce oxidative stress. The antioxidant qualities of these doped QDs help to reduce oxidative stress, which is linked to a number of grave health problems.[24,25] Including photodetector fabrication using as-prepared doped nanomaterials and testing its performance, a proper investigation of the interactions between nanocatalysts and pollutants is also essential, which helps to improve the efficacy of the photocatalytic abilities of nanocatalysts. One commonly used isothermal titration calorimetry (ITC) technique can be employed in this regard.[26,27] To investigate absorption cross-section and electric field intensity, we have applied the FDTD method.[28]

This work aims to fabricate a photodetector with enhanced photoactive properties using novel semiconducting nanomaterials and explore other possible applications. In this regard, we have synthesized three doped QDs samples, *i.e.*, Ag-doped SnO_2 QDs having the composition $Ag_xSn_{1-x}O_2$ ($x = 0.00$, 0.03, and 0.06) using wet chemical co-precipitation approach and thoroughly investigated the photoactive properties for photodetector application, antioxidant properties, physical properties and interactions between as-prepared nanocatalysts and *p*-nitrophenol. It was observed that substituting silver ions heavily altered the microstructural, optical, antioxidant, and interaction properties of pure SnO_2 QDs. Dopant Ag ions have tailored the band gap of the host nanomaterial, which supports in modifying the photoactive responses for photodetector application. We showed that, in comparison to the undoped system, optimal Ag doping in SnO_2 QDs enhanced antioxidant, photoactive and interaction properties efficiently. By tuning the physical properties of SnO_2 QDs *via* Ag-doping, an advanced photodetector with enhanced performance is tried to fabricate, along with a brief overview of the structure of photodetector devices. Additionally, this research makes appropriate linkages between microstructural, optical, and antioxidant properties of silver-doped SnO_2 QDs.

2. Experimental details

2.1. Preparation of pure SnO_2 QDs and silver-doped SnO_2 QDs

In order to prepare pure and Ag-doped SnO_2 QDs, the standard chemical co-precipitation method has been employed.[12–16] Three samples were synthesized with varying Ag content, which were designated as Ag-00 (SnO_2), Ag-03 (SnO_2), and Ag-06 (SnO_2), respectively. The synthesis technique has been discussed in detail in the ESI† section of this paper.

2.2. Photodetector device fabrication

To demonstrate the applications of the synthesized nanoparticles, we fabricated photodetectors with an ITO/

nanoparticles/Cu architecture. The indium-doped tin oxide (ITO) coated glass substrates were prepared using a standard cleaning protocol. Initially, the substrates were washed with a soap solution and subsequently ultrasonicated for 15 minutes each in deionized water, acetone, and isopropyl alcohol (IPA).[29–31] After cleaning, the ITO substrates were dried in a vacuum oven at 100 °C for 1 hour, followed by a 15 minute ozone treatment to ensure surface cleanliness.

The complete device fabrication process has been shown in Scheme S1 (in ESI†). A 4.5 mg ml^{-1} solution in ethanol was prepared and stirred on a hot plate at 60 °C for 12–14 hours. The precursor solution was then spin-coated onto pre-cleaned ITO and n-Si substrates at 2000 rpm for 30 seconds. The deposited thin films were annealed at 100 °C for 30 minutes. A 50–60 nm layer of SnO_2 QDs has been obtained, and a cross-sectional image of SnO_2 QD thin films was also captured. Finally, a 100 nm copper metal electrode was deposited by a thermal evaporator with a base pressure of 1×10^{-6} mbar to complete the device fabrication process. For Si substrates, an 80 nm thick Au layer was deposited, followed by a 20 nm Ti layer to enhance adhesion. Further, the fabricated devices were characterized using a Keithley 2470 electric source meter for current–voltage measurements. The devices were illuminated by a 200 nm optical fiber source integrated with a deuterium lamp.

2.3. Isothermal titration calorimetry (ITC) analysis

ITC experiments were performed on a MicroCal PEAQ-ITC, Malvern Analytical, at 25 °C. In the typical experiments, 40 μL of each dispersed solution of bare SnO_2 QDs (3 mM), and 6% Ag doped SnO_2 QDs (7.7 mM) in the syringe were injected separately to equal steps of 2 μL into 280 μL of a 0.1 mM of *para*-nitrophenol in the cell.[26,27] The nanoparticles were titrated with 19 injections (volume of 2 μL) and the time interval between two consecutive injections was maintained at 150 s, in order to obtain a systematic and complete return to baseline with an agitation speed of 750 rpm. The heat generated during titration after each injection was recorded. All the details regarding ITC analysis can be found in the ESI† section.

2.4. Measurement of antioxidant activity

The antioxidant property of as-prepared QDs was investigated with the aid of 2,2-diphenylpicrylhydrazyl (DPPH) scavenging experiment.[24,25] The entire procedure has been discussed in the ESI† section of this manuscript.

2.5. Characterization techniques

All the characterization techniques used to investigate the synthesized QDs have been discussed briefly in the ESI† section of this paper.

3. Results and discussion

3.1. Powder X-ray diffraction (P-XRD) analysis

A potential technique for figuring out the crystal structure, phase purity, and crystallite size of a material is X-ray diffraction (XRD) method. The XRD patterns of $Sn_{1-x}Ag_xO_2$ quantum dots (QDs) at 300 K were recorded, containing different concentrations of silver ions ($x = 0$, 3, and 6%) and is shown in Fig. 1. These patterns provide important light on the chemical and physical characteristics of the materials that were produced. According to the XRD study, the QDs have a tetragonal rutile crystal structure that is in line with JCPDS card number 41–1445, which denotes a certain arrangement of atoms inside the lattice. The crystallographic phase purity of prepared QD samples was confirmed by the lack of any other peaks in the XRD profiles other than those associated with the main tin rutile phase.[10–16] This feature is essential since it guarantees that the materials are devoid of contaminants or extra phases. Furthermore, the broadening of XRD diffractogram peaks implies that the produced materials are nanocrystalline and nanosized in nature. A number of variables, including crystallite size, microstrain in tiny crystals, and instrumental effects, can be accountable for the XRD peaks broadening.[32] By measuring the Full Width at Half Maximum (FWHM) of the intense (110) peak, and then by using Scherrer's method, we have obtained the average size of the nanocrystallites with the help of stated equation[31,33]

$$D = \frac{0.89\lambda}{\beta \cos \theta} \quad (1)$$

The produced materials were shown to exhibit quantum confinement effects, as evidenced by the average crystallite size of each sample consistently being determined to be below the Bohr excitonic diameter (5.4 nm) for SnO_2 nanomaterials[14] (see Table 1).

This implies that the distinct size-dependent characteristics result from the quantum confinement of the charge carriers inside their nanocrystalline structure of the material. Furthermore, using the Miller indices and the stated relation below, the lattice constants (a, b and c) of the unit cell for all $Ag_xSn_{1-x}O_2$ QDs were determined[33] (see Table 1).

$$\frac{1}{d^2} = \frac{h^2 + k^2}{a^2} + \frac{l^2}{c^2} \quad (2)$$

It was found that the lattice constant grew steadily as the amount of Ag in the nanocrystals increased. The mismatch in ionic radii between Ag^{2+} and Sn^{4+} ions is thought to be the cause of this phenomenon, wherein the lattice constant changes when Ag^{2+} ions are substituted inside the SnO_2 structure.[31–34] Ag ions have comparatively larger diameter than Sn ions, therefore the substitution of Ag ions in SnO_2 matrix hindered the crystal growth. The oxygen vacancies also produced in the doped samples to compensate the valency. These two combined effects resulted in reduction of mean size of the doped samples, which is reflected in XRD patterns as a result of peak broadening. Lowering of crystalline nature and several surface effects due to reduction in size with increasing Ag dopant concentration also led to broadening in XRD peaks with low intensity. We have also measured the hydrodynamic diameter of each QD sample using DLS measurement and the values were obtained as 5.46 nm [Ag-00 (SnO_2)], 4.32 nm [Ag-03 (SnO_2)], and 1.98 nm [Ag-06 (SnO_2)]

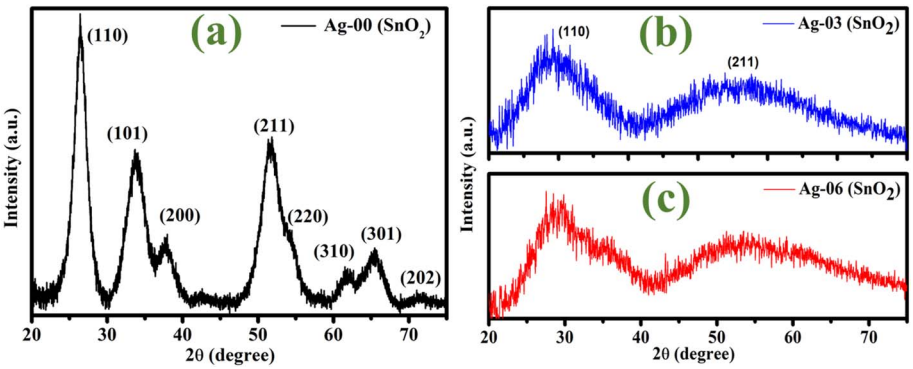

Fig. 1 P-XRD patterns of (a) Ag-00 (SnO_2), (b) Ag-03 (SnO_2), and (c) Ag-06 (SnO_2) QDs.

Table 1 Contains unit cell parameters of all the QD samples

Sample Id	D (nm)	$a = b$ (Å)	c (Å)
Ag-00 (SnO_2)	3.4	4.73	3.41
Ag-03 (SnO_2)	3.0	4.71	3.39
Ag-06 (SnO_2)	2.9	4.69	3.37

respectively as seen from Fig. S1 (in ESI†). The obtained values of hydrodynamic diameter were found to be comparable with the Bohr excitonic diameter, which confirmed the QDs nature of prepared samples.

3.2. TEM image analysis

High-resolution transmission electron microscope (HRTEM) pictures of both pure and doped quantum dots (QDs) are shown in Fig. 2(a–c). The photos demonstrate the synthesized QD accumulation, which is probably caused by van der Waals forces and interparticle interactions.[32] This emphasizes how crucial it is to comprehend the behavior of these particles at the nanoscale. The QDs continually display a nearly spherical form despite this buildup, indicating the accuracy of the production process. A thorough examination of the mean particle size and average size distribution of both pristine and doped SnO_2 QDs can be found in the inset histograms in the HRTEM pictures. The average particle size for the Ag-00 (SnO_2) sample is 3.61 nm, but the Ag-03 (SnO_2) and Ag-06 (SnO_2) samples had average particle sizes of 3.53 nm and 3.36 nm, respectively. The strong quantum confinement of excitons within the QDs is supported by the average particle sizes, which closely resemble the mean crystallite size.[32,35] Additionally, the micrographs exhibit remarkable size and shape homogeneity, indicating exact control throughout the synthesis process. By designating each ring in the SAED pattern [see Fig. 2(d)] with its associated Miller indices. A high-resolution TEM image of Ag-06 (SnO_2) sample has been also captured to show the QD nature [see Fig. 2(e) and (f)]. This emphasize the crystalline form of the nanomaterial and offers details on its structural integrity and possible uses, adding to the clarity of the picture. Furthermore, as Fig. 2(f) illustrates, the interplanar distance measured in the (110) plane is 3.40 Å, shedding light on the crystalline structure of the QDs. The crystalline structure of Ag-06 (SnO_2) QDs is confirmed by the concentric circular rings visible in their Selected Area Electron Diffraction (SAED) pattern.[14] These conclusions are further supported by the observed tetragonal rutile crystal structure, which is compatible with the HRTEM pictures and other investigations.[33] Our comprehension of the structure of the synthesized QDs and their possible applications in optoelectronics and catalysis is improved by this structural insight.

3.3. UV-visible spectra studies

Understanding the optical bandgap of semiconducting nanomaterials is essential to comprehending their optical and electrical characteristics. This bandgap is very essential for both pure and doped SnO_2 quantum dots (QDs) and is usually determined using UV-visible absorption spectra, which cover the range of 100–1000 nm.[36] These spectra shed light on the room-temperature direct and indirect optical transitions of the QDs. At 300 K, the direct bandgap of pure SnO_2 is 3.62 eV; however, because of quantum confinement effects, this bandgap marginally reduces in nanoscale quantum dots.[14] Using the Tauc relation, the optical bandgap of both doped and undoped SnO_2 QDs is found[32,36]

$$\alpha(\nu)h\nu = B(h\nu - E_0)^n \quad (3)$$

Several factors are involved in the Tauc relation, including 'B' (an arbitrary constant), 'E_0' (the energy for the direct optical transition of QDs), 'α' (the absorption coefficient), and 'n' (the index). The index 'n' is 1.5 for indirect bandgap transitions and 0.5 for direct bandgap transitions. Using particular formulae, the absorption coefficient 'α' for the QDs is ascertained from the collected absorbance (A) data.[36]

$$I = I_o\, e^{-\alpha d} \text{ and } A = \log_{10}(I_o/I) \quad (4)$$

Here, the absorption coefficient 'α' may be written as $\alpha = 2.303(A/d)$, where 'd' marks the tube thickness. For direct bandgap transitions, plot $(\alpha h\nu)^2$ *versus* photon energy ($h\nu$) to construct a Tauc plot using the calculated α values. This Tauc plot represents the connection between $(\alpha h\nu)^2$ and ($h\nu$) for both pure and doped SnO_2 QDs, is displayed in Fig. S2.† Ag-00

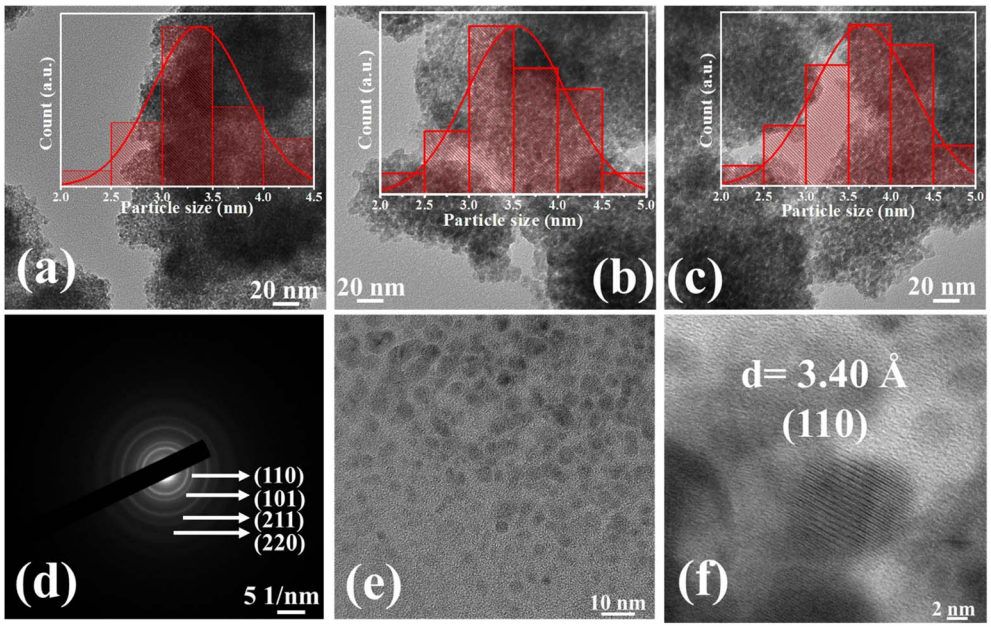

Fig. 2 HRTEM images of (a) Ag-00 (SnO_2), (b) Ag-03 (SnO_2), and (c) Ag-06 (SnO_2) QDs, (d–f) SAED pattern, distinguish QDs and interplanar spacing of Ag-06 (SnO_2) QDs.

(SnO_2), Ag-03 (SnO_2), and Ag-06 (SnO_2) QDs have computed E_0 values of 3.23 eV, 3.37 eV, and 3.46 eV, in that order. The main causes of the energy gap increases between the samples, which went from 3.23 eV to 3.46 eV, are quantum confinement effects and interactions (S2P interaction) between the valence or conduction bands of SnO_2 QDs and the s electrons in silver ions.[32] Higher Ag concentration was also associated with a significant blueshift in electromagnetic wave absorption, demonstrating the impact of doping on the optical characteristics of SnO_2 QDs. All things considered, the synthesized QDs show good absorption properties of both UV and visible light, which makes them appropriate for a wide range of optical applications. The perpendicular alignment of dipoles between particles during two separate vibrational modes of optical stimulation was shown to be responsible for the shift of absorption peaks to higher energy with increasing Ag concentration in SnO_2. A substantial interaction between the Ag and SnO_2 quantum dots is suggested by this change. The perpendicular alignment of dipoles between particles during two separate vibrational modes of optical stimulation was shown to be responsible for the shift of absorption peaks to higher energy with increasing Ag concentration in SnO_2.[37] A substantial interaction between the Ag and SnO_2 quantum dots is suggested by this change.

3.4 FDTD analysis

Using UV-vis spectroscopy is a useful method to investigate how doping affects the optical characteristics of SnO_2 QDs. Assimilation primarily addresses electron excitation from the valence band to the conduction band. The picture displays the UV-reproduced retention spectra of undoped and Ag-doped SnO_2 QDs.[36–39] The assimilation peaks of undoped SnO_2 QDs are seen to be at 348 nm, which is blue-shifted in comparison to the mass band hole of SnO_2, due to the influence of quantum limitation. The retention peak of Ag-doped SnO_2 QDs is also shifted to higher frequencies in contrast to undoped SnO_2. This movement results from the band-hole energy being lowered by Ag doping in the SnO_2 grid structure. Ag-03 (SnO_2) and Ag-06 (SnO_2) assimilation tops are seen in Fig. 3 at 352 and 354 nm, respectively. The increase in electric field force from 85.3 to 87.9 (V m^{-2}) observed following silver doping into SnO_2 QDs is shown in Fig. 4. Our findings show that SnO_2 QDs have an electric field power of 11.5 (V m^{-2}) respectively.[39,40] When silver is present in the quantum dots, the dielectric medium surrounding the SnO_2 QD nanostructures changes, leading to enhancements in the optical range and field strengths. Because

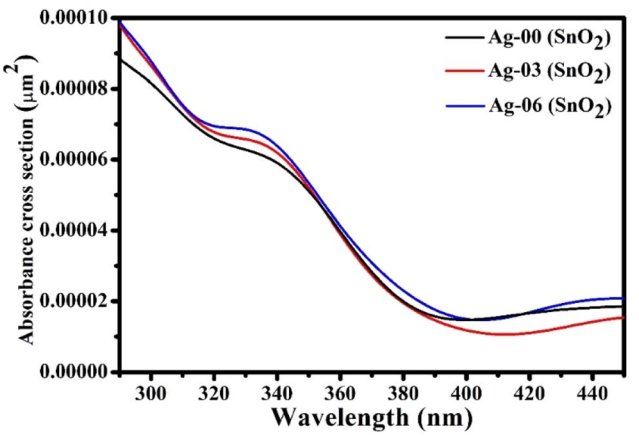

Fig. 3 Absorption cross-section of SnO_2 QDs and Ag-doped SnO_2 QDs.

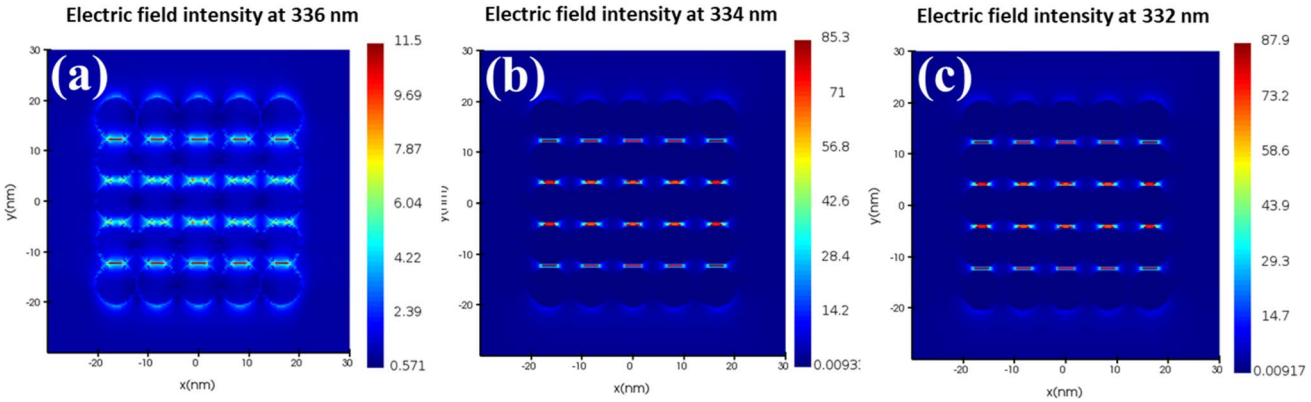

Fig. 4 Electric field intensity profile of (a) Ag-00 (SnO_2), (b) Ag-03 (SnO_2), and (c) Ag-06 (SnO_2) QDs.

the plasma recurrence of the conduction electrons in the Ag nanostructure is within the detectable reach, Ag exhibits solid assimilation in the apparent area of the electromagnetic range. The material dissipates and produces hot transporters, or hot electrons, due to the high retention, which is linked to an enhancement of the electric field around the impetus. Because of the high-rate Ag nanostructures, interparticle plasmonic communication plays a major role in the further improvement of field powers. Furthermore, depending on the kind of particles, there are certain locations referred to as plasmonic zones of interest where the improvement factor achieves its maximum value. The nanoscale gaps between particles are usually where the regions of interest are located. The expanded reactant movement is mostly the result of these gaps. The electric field enhances the photocatalytic action and increases the response rates at these holes. Reactant improvement is seen to grow quadratically with the local real light force, indicating the collaboration of hot electrons in the upgrade component induced by plasmon excitation. The nanostructure geometry and local electric field enhancement are found and correlate with catalytic improvement.[41] The electron energy distribution function is directly impacted by this changing electric field, which in turn impacts the reaction rates.

3.5. Fourier transform infrared spectroscopy (FTIR) spectra studies

An efficient analytical method for detecting compounds and locating different functional groups and chemical bonds in materials is Fourier Transform Infrared Spectroscopy (FTIR). By exposing materials to infrared light, this technique analyzes them over the electromagnetic spectrum and essentially creates a distinct "fingerprint" of their chemical properties.[36,42–44] FTIR spectra of undoped, 3%, and 6% silver-doped tin oxide (SnO_2) quantum dots (QDs) in the 400–4000 cm^{-1} range were obtained in a recent study. The findings, which are shown in Fig. 5(A), offer important new information on the molecular makeup and structural characteristics of these materials.[44,45] The existence of SnO_2 in the materials under analysis was confirmed by the FTIR spectra, which showed unique peaks corresponding to various chemical functionalities in all samples. The stretching modes of OH^- ions trapped in the crystals are responsible for the band seen between 3000 and 4000 cm^{-1}, which indicates the existence of adsorbed water and Sn–O groups. In addition, peaks in the 1418–1622 cm^{-1} region are indicative of both symmetric and asymmetric C–O bond stretching, which sheds light on the samples' chemical makeup. The constant discovery of unique SnO_2 peaks in the 600 cm^{-1} to 1300 cm^{-1} region for all samples is an important finding from the FTIR study. Interestingly, the peak at 937 cm^{-1}, which is connected to the symmetric stretching of Sn–O–Sn bonds, does not alter much even after Ag ions are added to the quantum dots.[14] This discovery implies that the essential structural characteristics of SnO_2 are not considerably affected by the addition of Ag dopants. Changes in the mass of the quantum dots, which may modify vibrational frequencies, as well as modifications to the bond's spring constant and length, might be responsible for the slight fluctuations in the peak related to Sn–O–Sn bond stretching following Ag insertion.[32] These features draw attention to the complex interplay between the structural and chemical characteristics of the materials and underscore how important it is to comprehend how dopants affect the host material's vibrational properties.

3.6. Photoluminescence spectra studies

Room-temperature photoluminescence spectroscopy is a valuable tool for studying the optical properties of materials and the electron transfer and recombination rate of photogenerated electron and hole pair, and it has been particularly useful in investigating the behavior of semiconductor quantum dots. In Fig. 5(B), the room-temperature photoluminescence spectra of SnO_2 QDs and Ag-doped SnO_2 QDs are presented. This data reveals interesting findings about the effects of silver doping on the photoluminescence properties of these quantum dots.[13–16] The pristine spectra show the broad visible emission peaks at 588 nm due to the crystalline defects during the growth process inside SnO_2, high concentrations of tin interstitials or oxygen vacancies produce defect levels inside the band gap. Significant photoluminescence (PL) emissions are produced as a result of the interactions between these oxygen vacancies and tin interstitials, which create a large number of trapped states or metastable

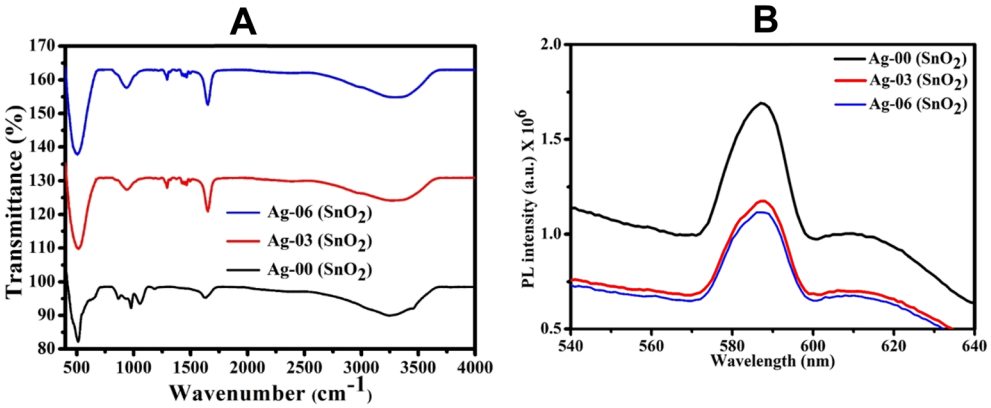

Fig. 5 (A) Stacked FTIR spectra (B) photoluminescence spectra of SnO_2 QDs and Ag-doped SnO_2 QDs.

energy levels.[45] Small grain boundaries can also act as efficient luminescent centers, which promotes the recombination of photogenerated carriers inside SnO_2, high concentrations of tin interstitials or oxygen vacancies produce defect levels inside the band gap. Significant photoluminescence (PL) emissions are produced as a result of the interactions between these oxygen vacancies and tin interstitials, which create a large number of trapped states or metastable energy levels. Small grain boundaries can also act as efficient luminescent centers, which promotes the recombination of photogenerated carriers. When compared to pure SnO_2, all Ag–SnO_2 samples show lower PL intensity, which suggests improved charge separation and less electron–hole recombination. Ag is essential for effectively separating charges from SnO_2 because it traps photogenerated electrons; this is further evidenced by the enhanced visible light performance of Ag–SnO_2 QDs.[14,45,46] Ag-06 has the lowest PL intensity of all the Ag–SnO_2 samples that were generated, indicating that it is the best photocatalyst in terms of photocatalytic activity. The photogenerated electron–hole pairs of Ag–SnO_2 QDs are efficiently separated, as seen by the PL emission from the compound.

3.7. SEM analysis

Fig. 6(a) and (b) displays the FESEM pictures and the energy-dispersive X-ray spectroscopy (EDS) analysis of the Ag-doped SnO_2 quantum dots (Ag-06) and the pristine SnO_2 quantum dots. The pictures show that the particles have a spherical shape and are uniformly dispersed.[47] Furthermore, the existence of every element in the synthetic samples was verified by the EDS spectra. This comprehensive examination confirms that particular components were present in the prepared samples and nanoparticles formed. We have captured the FESEM image of the fabricated device to estimate the thinkness of the QDs on the ITO substrate. The thickness of the obtained SnO_2 QDs has been evaluated in the range of 50–60 nm, which is shown in Fig. S4.†

3.8. BET analysis

The BET analysis looks at the physical adsorption and desorption of nitrogen gas molecules to determine the surface shape, porous structure, and specific surface area of the produced nanomaterials. The surface area of nanomaterial is essential to its possible uses since a bigger surface area provides more active sites and improves interactions with analytes. At 18 hours, all samples were kept at 200 °C with a nitrogen gas flow to acquire the adsorption–desorption isotherms.[47] The surface area and porosity of the three nanocatalysts were measured using the nitrogen adsorption–desorption isotherms, as indicated in Fig. 7(a–c). The adsorption curve climbed steadily in the low-pressure area before rising sharply when P/P_0 approached 0.80, as seen by the isotherms.[48] The isotherms of all the nanocatalysts showed close alignment with a standard type IV adsorption isotherm, suggesting the existence of a mesoporous structure. For Ag-00 (SnO_2), the specific surface areas were measured to be 48.14 $m^2\ g^{-1}$, Ag-03 (SnO_2) to be 63.44 $m^2\ g^{-1}$, and Ag-06 (SnO_2) to be 84.83 $m^2\ g^{-1}$ [see Fig. 7(d)]. When compared to pristine and other doped samples, the 6% Ag-doped SnO_2 QDs had the most surface area. It may be inferred from this that adding Ag ions to SnO_2 nanocrystals facilitates better dispersion in solution and increases interaction activity. The picture shows a histogram that shows the specific surface area of each sample dependent on pore radius.[36] The Ag-06 sample is expected to have more active sites for a variety of applications because of its higher specific surface area.

3.9. Raman spectra analysis

Raman spectroscopy is a method used to examine the structural defect and crystallinity of materials. Raman spectra of all the samples was registered using a laser of wavelength 532 nm, is depicted in Fig. 8. The Raman spectrum and the Raman band were fitted using the Lorentzian function.[16] The tetragonal rutile structure of SnO_2 QDs is confirmed by the measured Raman vibrational modes E_g, A_{1g}, and B_{2g}, which are located at 481, 622, and 769 cm^{-1}, respectively. For Raman forbidden, the B_{1u} mode is represented by the mode at 551 cm^{-1}. The modes 246 and 298 cm^{-1} are represented by the E_u (TO) and E_u (LO) modes that occurred due to the tiny size effect of SnO_2 QDs.[42,44] TO stands for transverse-optical vibration, and LO for longitudinal-optical vibration. Because of the greater peak intensity and smaller peak breadth, the SnO_2 QDs exhibit a higher

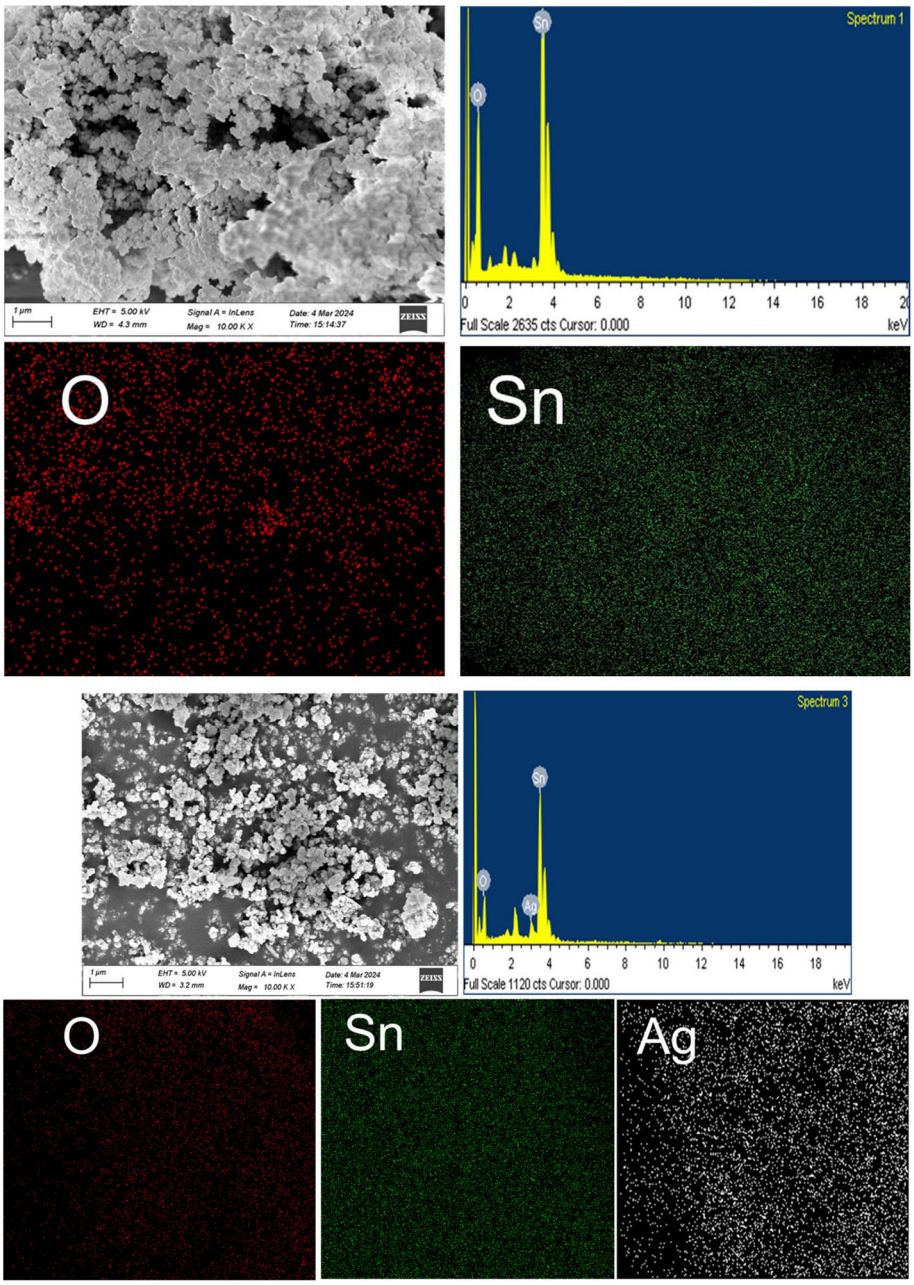

Fig. 6 (a) Pure SnO_2 QDs SEM image. (b) Ag-doped SnO_2 QDs [Ag-06(SnO_2)] SEM image.

crystallinity nature than the Ag-doped SnO_2 QDs. Ag-doped SnO_2 QDs Raman spectra show a shift in the Raman peaks when compared to the pure SnO_2 QDs.[49,50] The shift in Ag-doped SnO_2 Raman spectra was the cause of the lattice disorder. The size of Ag-doped SnO_2 QDs was reduced due to the expansion of Raman peaks. The undefine peak displays the phonon confinement effect. It could cause the migration of Sn ions in the interstitial locations.[16] In comparison to the pristine SnO_2 QDs, the particle size is lower after doping, according to the XRD analysis.

3.10. Electrical properties through Hall effect measurement

For characterizing a semiconducting nanomaterial, the Hall effect is most commonly used technique. It provides accurately the information regarding the type of charge carriers, mobility and carrier density of a semiconducting material. Several parameters such as mobility, resistivity, conductivity, bulk concentration, sheet concentration, average Hall coefficient, and sheet resistance were measured using Hall effect measurement system in a magnetic field for both the pristine SnO_2 QDs and Ag-doped SnO_2 QDs. All of the Hall Effect parameters were estimated using the physical equations listed

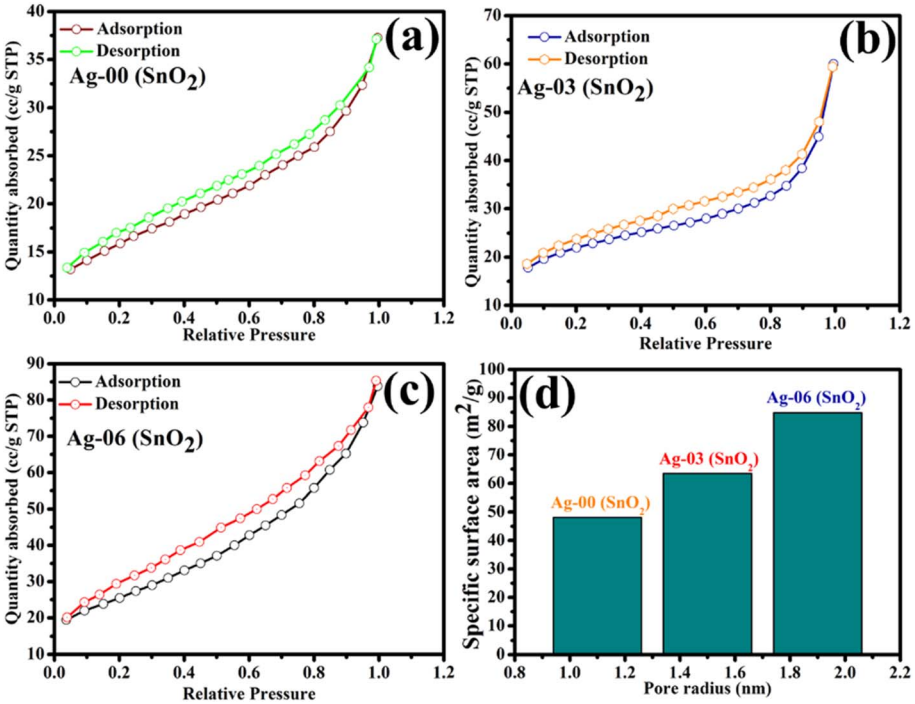

Fig. 7 (a–c) N_2 adsorption–desorption isotherms of all the samples and (d) histogram of the specific surface against pore radius.

below.[51–53] The sheet density (n_s/cm^3) of the semiconductor charge carrier was calculated using the Hall voltage (V_H) and the known values of the magnetic field and current.

$$n_s = 8 \times 10^{-8} \frac{IB}{qV_H} \quad (5)$$

where q is the elementary charge (1.602×10^{-19} C), I denote the current, B is the magnetic field, and V_H is the Hall voltage,

$$n = \frac{n_s}{t} \quad (6)$$

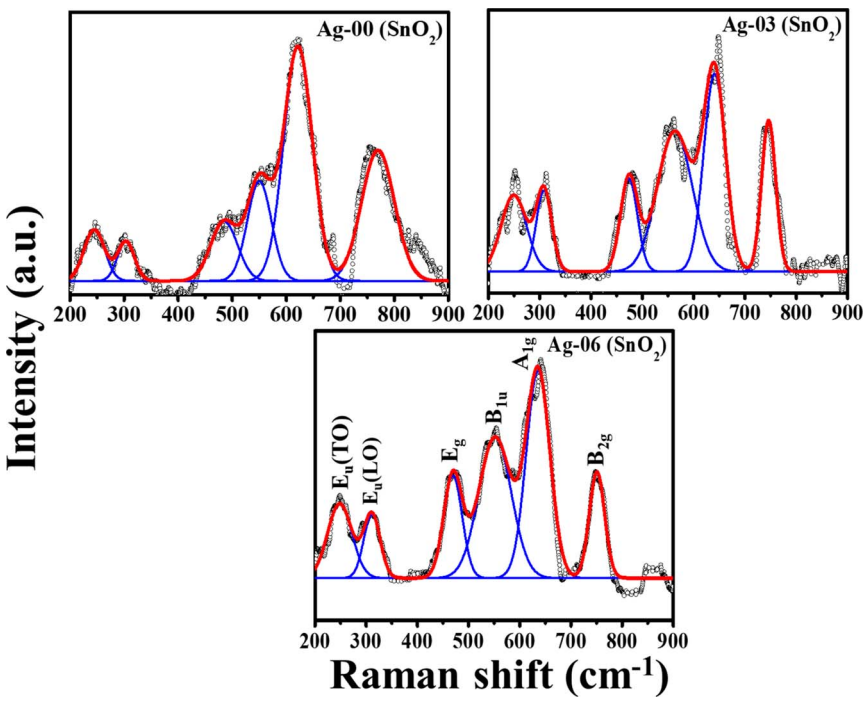

Fig. 8 Raman spectra of all the synthesized QDs recorded at 300 K.

Table 2 Displays several Hall effect parameters

Sample Id	Ag-00 (SnO_2)	Ag-03 (SnO_2)	Ag-06 (SnO_2)
Bulk concentration (cm^{-3}) $\times 10^{14}$	7.01	−1.16	−2.59
Sheet concentration (cm^{-3}) $\times 10^{13}$	3.51	−0.58	−1.29
Sheet resistance (Ω) $\times 10^{4}$	1.10	21.10	9.55
Resistivity (Ω cm)	5.50×10^{2}	1.06×10^{4}	4.78×10^{3}
Conductivity (Ω cm)	1.82×10^{-3}	5.97×10^{-4}	3.82×10^{-4}
Mobility ($cm^2\ V^{-1}\ s^{-1}$)	20.9	32.6	8.89
Hall coefficient ($cm^3\ C^{-1}$) $\times 10^{4}$	1.12	−5.37	−3.89

Here, t stands for the sample's thickness. The sheet resistance (R_s), as determined by the Vander Pauw (VDP) technique, is as follows[51,52]

$$2e^{-R/R_S} = 1 \quad (7)$$

R is the average resistance between the synthesized nanomaterials in this case. Resistivity (ρ) of the materials was determined by

$$\rho = R_s t \quad (8)$$

Using the following equation, we calculated the Hall mobility ($cm^2\ V^{-1}\ s^{-1}$) from the R_s and t values

$$\mu = \frac{1}{qn_sR_s} = \frac{|V_H|}{IBR_s} \quad (9)$$

Again, calculate the Hall coefficient by using this equation[53]

$$RH = \rho v = \frac{1}{qn_sR_s} = \frac{t\ V_H}{IB} \quad (10)$$

The conductivity and carrier types were determined by the Hall coefficient (R_H). The n-type flow of electrons is represented by the negative R_H values, while the p-type flow of holes is represented by the positive R_H values. We calculated the conductivity using the stated formula

$$\sigma_c = \frac{t}{RA} \quad (11)$$

Here, R and A are measured resistance and area of the electrode. Table 2 includes all of the observed Hall effect parameters: sheet concentration, conductivity, mobility, resistivity, bulk

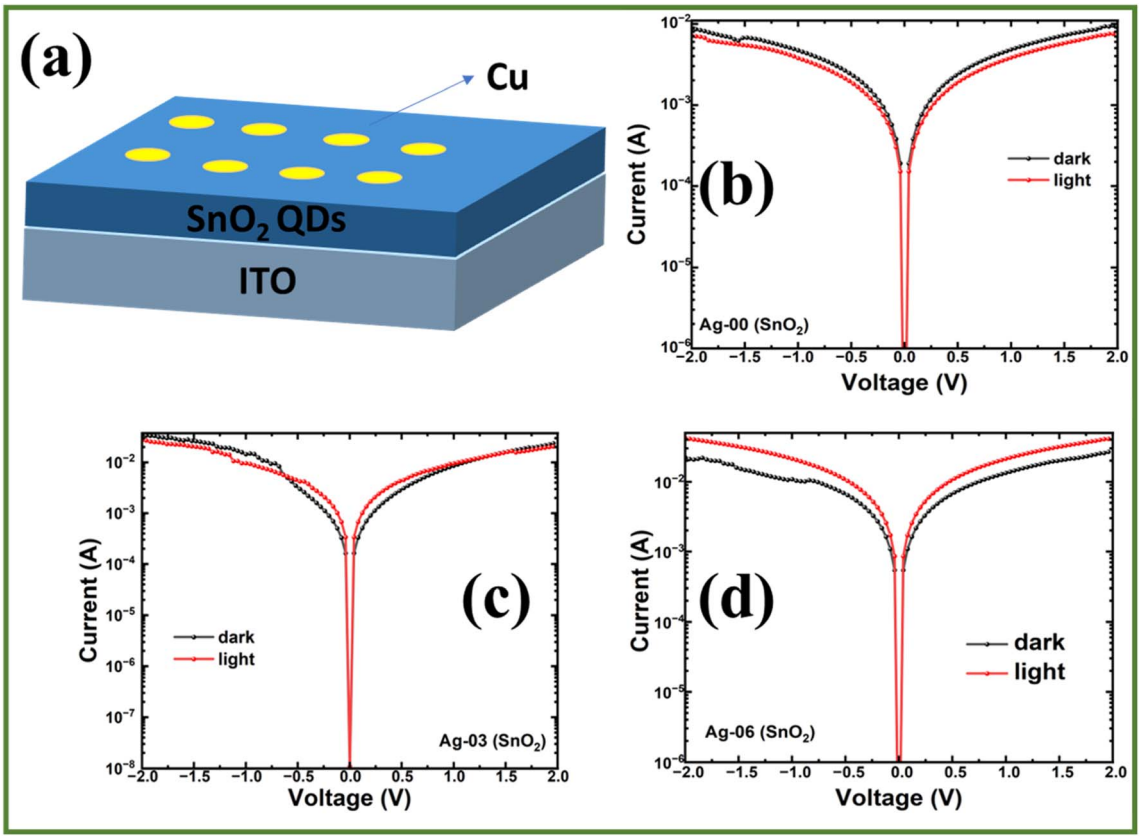

Fig. 9 (a) Schematic device configuration of ITO/SnO_2 QDs/Cu detectors with their (b–d) current–voltage characteristics under dark and light conditions.

concentration, and Hall coefficients.[51–53] It is established that SnO_2 is a p-type semiconductor based on the Hall effect data when the tin is replaced by silver atoms, indicating that Ag-03 (SnO_2) and Ag-06 (SnO_2) exhibit n-type behavior. Silver is an excellent conducting metal with significant number of free electrons and low resistivity. Doping of Ag ions in the SnO_2 matrix within percolation limit, increase the number density of free electrons and have the capacity to transform the p-type pure SnO_2 QDs into n-type semiconducting nanomaterial. Room temperature Hall effect experiment revealed that the pure SnO_2 QDs showed the p-type semiconducting nature, whereas with the addition of metal Ag ions, electrons became the majority charge carriers and the doped SnO_2 QDs turned into n-type semiconductors.

3.11. Performance of fabricated photodetectors

The schematic device configuration of SnO_2 QDs and Ag-doped SnO_2 QDs photodetectors has been represented in Fig. 9 and 10 respectively. Fig. 9 depicts the current–voltage characteristics of fabricated devices in ITO/QDs/Cu. All the fabricated devices on ITO substrates depict ohmic characteristics, which have been improved upon light illumination. Our device structure, ITO/QDs/Cu, does not inherently form a strong rectifying junction at the metal–semiconductor interfaces. Instead, the contacts are quasi-ohmic, resulting in a predominantly linear *I–V* behavior in dark and illuminated conditions. The linear, *i.e.*, ohmic response is characteristic of photoconductive detectors, where the photocurrent increases under illumination due to enhanced photoconductivity and has been observed in several reports.[3,54–56]

Another possible reason for the ITO/QDs/Cu devices exhibiting ohmic characteristics can be attributed to the comparable work functions of the electrodes. ITO is a transparent conducting oxide which typically has a work function in the range of 4.2–5.0 eV, while copper (Cu) has a work function of approximately 4.5 eV.[57,58] The near-similar work function between substrate and metal electrode can reduce the built-in potential and barrier height, which promotes efficient charge carrier injection and extraction at the interfaces, minimizing the energy barrier and supporting ohmic contact formation.[59,60] To further validate these findings, we have also fabricated devices with Si/QDs/Au configuration, which exhibited a consistent trend (see Fig. 10). Pristine SnO_2 QDs showed ohmic characteristics, which shifted to Schottky-type behavior upon Ag doping, see Fig. 10(b) and (c). This systematic modulation in electrical characteristics across different device architectures confirms the Ag-induced p-to-n type transition in SnO_2 QDs and its consequential influence on interfacial charge transport processes.[61,62]

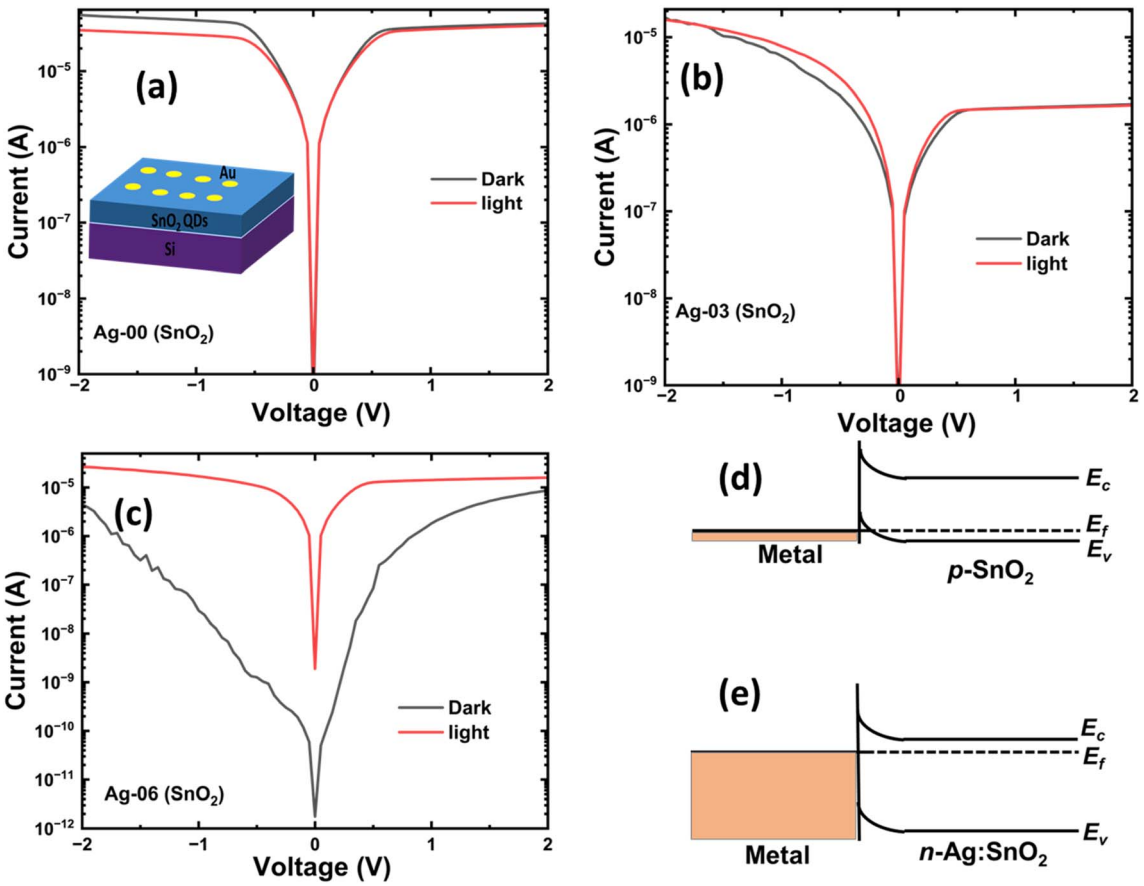

Fig. 10 (a–c) Current–voltage characteristics of SnO_2 devices under dark and light conditions. Inset of 10 (a) depicts the schematic device configuration of Si/SnO_2 (d) and (e) energy band diagram of SnO_2 and Ag modified SnO_2 devices.

Thus, in our study, SnO_2 QDs exhibited p-type conductivity, where holes act as the majority charge carriers. When a metal with a lower work function than p-type SnO_2 is brought into contact with it, an ohmic contact is generally formed (see Fig. 10(d)). This allows for efficient, low-resistance charge injection and extraction of holes, resulting in a linear current–voltage relationship.[59] However, upon doping SnO_2 QDs with Ag, the conductivity type of the material shifts to n-type, where electrons become the majority charge carriers. This transition is typically attributed to Ag incorporation, either occupying interstitial sites or substituting tin (Sn) sites in a manner that donates free electrons to the conduction band, or modulates the defect landscape (*e.g.*, reducing hole-generating defects like tin vacancies or increasing electron-donating oxygen vacancies). For n-type Ag modified SnO_2, a metal with a lower work function than the semiconductor (such as Cu in this case) forms an ohmic contact. This again results in a linear *I–V* characteristic due to the efficient injection and extraction of electrons without significant barrier formation.[59] Conversely, a metal with a higher work function (Au, ~5.1 eV) forms a Schottky barrier with n-type semiconductors, leading to rectifying (non-linear) behavior. The energy band diagram of metal semiconductor junction is shown in Fig. 10(d) and (e).

At reverse bias (−1 V) in ITO/QDs/Cu devices, the dark current (I_{dark}) is 4.71 mA, 14.43 mA, and 10.87 mA for Ag-00 (SnO_2), Ag-03 (SnO_2), and Ag-06 (SnO_2), respectively. Upon UV light illumination (λ = 200 nm) of power (P_{in}, 1 μW cm^{-2}), photocurrent (I_{ph}) has been changed and observed to be 3.77 mA, 9.62 mA, and 21.35 mA for Ag-00, Ag-03, and Ag-06, respectively. However, at forward bias (1 V), the light-to-dark current ratio is significantly better and found to be 0.79, 1.11, and 1.59 for Ag-00, Ag-03, and Ag-06 devices, respectively. Whereas, Si/QDs/Au devices depict better photo response compared to ITO/QDs/Cu devices. The values of various device parameters of both devices have been summarized in Table 3.

The photoresponsivity (R) per unit area (A) of the devices has been evaluated using the following formula[29–31]

$$R = \frac{I_{ph} \sim I_{dark}}{AP_{in}} \quad (12)$$

Here, the effective device area (A) is 8.9×10^{-3} cm^2. Another figure of merit for light detection detectors is the percentage increase in photo-to-dark current ratio (PDCR), which can be defined as[63,64]

$$PDCR = \frac{I_{ph} \sim I_{dark}}{I_{dark}} \times 100\% \quad (13)$$

External quantum efficiency (EQE) of the devices can be evaluated using[30]

$$EQE = \frac{R \times hc}{q\lambda_{inc}} \times 100\% \quad (14)$$

Here, q is the electronic charge. Further, the photo detectivity (D) is given by[31]

$$D = \frac{R\sqrt{A}}{\sqrt{(2qI_{dark})}} \quad (15)$$

From Fig. 9(b) and 10(a), it can be observed that both the SnO_2 QD devices depict a negative photodetector behaviour. The negative photodetection in SnO_2 devices may appear due to various defect levels present in the SnO_2 energy levels, high oxygen, and moisture content, *etc.*[62–65] As confirmed by FTIR and PL emission spectra, SnO_2 QDs exhibit pronounced more OH content and PL broadening towards higher wavelengths, indicating a higher concentration of oxygen vacancies compared to Ag-modified SnO_2 QDs.[62] The lower oxygen vacancies reduce the concentration of conduction electrons in the device, creating an electron depletion layer. Therefore, the conductivity observed in Hall effect measurement and the dark current in Ag-modified SnO_2 devices are reduced, as seen in Fig. 9 and 10. The significant reduction in dark current in Ag-modified SnO_2 devices indicates the better detectivity of photodetectors. Further, the high value of detectivity is also attributed to the strong photo response and possible photoconductive gain effects in the present devices. Additionally, factors such as improved interface passivation, trap-assisted and photoconductive gain under illumination could collectively contribute to the enhanced detectivity observed despite the presence of elevated dark currents.[62–66]

Table 3 The photodetector parameters are compared to other UV photodetectors

Materials form	Bias (V)	λ (nm)	I_{ph} (μA)	R (mA W^{-1})	Reference
SnO_2 nanowire	5	310	0.0006	0.13	67
	12	365	130	—	68
	1	254	0.8	—	69
SnO_2 microwire	10	240	0.585	1.353×10^6 @ 300	54
		400	0.065		
SnO_2 nanobelt	−5	254	80	—	70
SnO_2 monolayer nanofilm	1	320	232.3	—	71
SnO_2 microstructures	3	315	0.002	7.1	72
	3	350	8	—	64
SnO_2 nanobranch	0.0004	365	0.0014	15	73
SnO_2 nanotubes	1	320	0.026	—	74
SnO_2 thin film	5	300	0.027	8	75
	1	290	0.66	4.9	76
	1	365	23.47	16.77	32
Ag-00 (SnO_2) quantum dots	**−1**	**200**	**30.1**	**1.89×10^6**	**Our work**

Table 4 Summary of device parameters

Devices	R (A W^{-1})	PDCR (%)	EQE (%)	D
ITO/Ag-00 : SnO_2 QDs/Cu	1.05×10^5	19.9	6.52×10^5	2.57×10^{14}
ITO/Ag-03 : SnO_2 QDs/Cu	5.40×10^5	33.3	3.35×10^6	1.88×10^{15}
ITO/Ag-06 : SnO_2 QDs/Cu	1.17×10^6	96.40	7.26×10^6	3.75×10^{15}
Si/Ag-00 : SnO_2 QDs/Au	1.89×10^3	35.80	6.43×10^3	4.60×10^{13}
Si/Ag-03 : SnO_2 QDs/Au	2.02×10^2	29.70	6.88×10^3	1.37×10^{13}
Si/Ag-06 : SnO_2 QDs/Au	1.90×10^3	57 800	6.45×10^3	1.85×10^{15}

In our case, the formula applied for detectivity is specifically valid under shot noise-limited conditions, where the primary noise source is the statistical fluctuation in the dark current. Since the value of dark current is significantly high, it is expected that the shot noise limited conditions are applicable in this case. This assumption is typically appropriate when shot noise dominates over other noise mechanisms such as thermal (Johnson) noise and 1/f noise, particularly at moderate to high frequencies and in devices with measurable dark currents. At present, due to instrumental limitations, we have not experimentally measured the noise values. However, we utilized this formula in the current work primarily to understand the relative trend of detectivity variation based on previous studies rather than to report absolute D^* values. The calculated detectivity trends offer qualitative insight into how Ag incorporation influences the SnO_2 optoelectronic performance.[66,67]

Further, among all devices, the Ag-06(SnO_2) device has a much higher photo-response due to its better charge carrier mobility. Moreover, the Ag-06(SnO_2) device has fewer defects, which reduces leakage current and improves its overall performance.[63,64] The improved photo response depends on the free electron concentration in the conduction band of metal-doped SnO_2, corresponding to the number of filled states. Hence, it can be understood that Ag doping also passivates the defect level in SnO_2. Table 4 contains all the device parameters. Further, the increased PDCR, EQE, and photo-detectivity in Ag-06 (SnO_2) photodetectors in both device configurations are due to optimal Ag doping, which improves charge separation and reduces the recombination of photogenerated electrons and holes. In pure SnO_2, optoelectronic defects like tin interstitials and oxygen vacancies act as traps, causing significant recombination and lower charge carrier efficiency, as discussed above.[29,64] When Ag is incorporated into SnO_2, it traps electrons and suppresses radiative recombination, resulting in much lower PL intensity, especially in Ag-06(SnO_2), which shows the best performance. The optimal amount of Ag in Ag-06(SnO_2) enhances charge carrier mobility and reduces defect-related losses, allowing more electrons to contribute to the photocurrent. This makes Ag-06(SnO_2) the most efficient among all samples for UV detection applications. We have compared our fabricated photodetector with the previously reported ones in Tables 3 and 5.

3.12. Charge transfer mechanism in SnO_2 photodetectors

A photodetector absorbs light and generates charge carriers in a semiconductor material. It behaves like a standard detector in the dark, with a dark current arising from thermally generated charge carriers.[82] In this state, SnO_2 adsorbs oxygen from the surrounding air, forming negatively charged oxygen ions on its surface, as shown in Fig. 11. These ions create a barrier restricting charge carrier movement, producing a dark current. When light with sufficient energy (equal to or greater than the bandgap of SnO_2) is incident on the material, photons are absorbed, exciting electrons from the valence band to the conduction band, creating electron–hole pairs. The internal electric field or an applied external bias separates these charge carriers, generating a photocurrent. Additionally, UV light causes the desorption of oxygen ions, releasing trapped electrons, further boosting the photocurrent, and passivating the optoelectronic defects of SnO_2.[32,83]

Incorporating silver (Ag) into SnO_2 significantly enhances the device's performance. Ag doping reduces surface recombination by passivating dangling bonds, promoting efficient charge separation, and changes the conductivity. The formation of a metal-semiconductor junction with Cu or Au electrodes improves the collection of electrons. Optimal Ag doping, especially in Ag-06 (SnO_2) quantum dots, enhances charge carrier mobility and minimizes defect-related losses, making it highly efficient for UV light detection. This combination of oxygen desorption, defect passivation, and improved carrier transport

Table 5 Comparison of Photodetector parameters of doped samples with other UV photodetectors

Materials form	Bias (V)	λ (nm)	I_{ph} (μA)	R (mA W^{-1})	Reference
SnO_2 : Ag/P–Si heterojunction	3	422	—	287	77
Optimized SnO_2 with Ag NPs TFT	1	365	—	309	78
Au NP-SnO_2	0.5	285	4200	1.6×10^6	79
AuNP/SnO_2/NiO	4.4 kV	365	10.6	3.53×10^{-3}	80
AuNP–SnO_2 nanowire	0.1	325	—	—	81
Ag-03 (SnO_2) and Ag-06 (SnO_2)	**−1**	**200**	**7.86**	**2.02×10^5**	**Our work**
	−1	**200**	**16.9**	**1.90×10^6**	

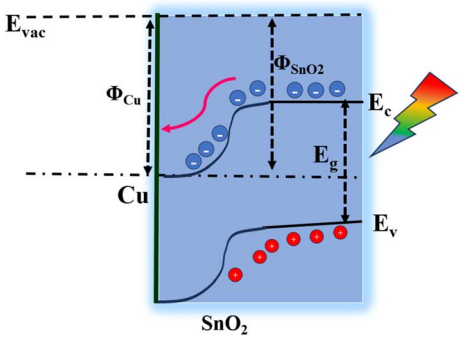

Fig. 11 Schematic energy band diagram of SnO_2 under the source.

results in superior performance and stability, positioning Ag-doped SnO_2 quantum dots as excellent emerging wide band gap semiconductors for UV detection.

3.13. Antioxidant activity analysis of Ag-doped SnO_2 QDs

After being left alone for a whole day, the stability of the DPPH solution was examined. At 517 nm, there is no change in the absorption's color or intensity. This implies that the DPPH solution did not change during the experiment. Ag lowers the absorbance at 517 nm doped SnO_2 QDs because they reduce the stable nitrogen free radical in 2,2-diphenyl-1-picrylhydrazyl (DPPH).[36,47] The electron density transfer from the oxygen atom to the odd electron on the nitrogen atom in DPPH, which results in a decrease in the intensity of the n* transition at 517 nm and a gradual change in the color of the DPPH solution from deep violet to colorless, may be responsible for the antioxidant activity of Ag doped SnO_2 QDs.[84]

Antioxidant activity of the synthesized NPs was investigated against its time of exposure. The solution's hue gradually changed from deep violet to colorless as the surface interactions between the Ag doped SnO_2 QDs and the DPPH solution progressed. According to UV-visible analysis, as exposure duration increased, the peak intensity of the supernatant DPPH solution at 517 nm steadily decreased (Fig. S7(A and B†)). The presence of Ag doped SnO_2 QDs allow for the visual monitoring of the antioxidant activity of the nanoparticles due to the color change of the DPPH solution and the degree of decrease in UV-visible peak intensity. The percentage antioxidant scavenging activity of the nanoparticles was computed using equation (i) as indicated in Fig. S7(C),† by measuring the UV-visible peak intensity of the control and the supernatant of the nanoparticles containing solution under examination at different time intervals.[36] From Fig. S7(C)† it is observed that the 6% Ag-doped SnO_2 shows the highest antioxidant activity in comparison to the 3% Ag-doped SnO_2 QDs. The bare Ag-00 (SnO_2) QD sample has negligible antioxidant activity as compared to Ag-doped SnO_2 QDs as shown in Fig. S8(A).† After 210 min of exposure time, Ag-03 (SnO_2) and Ag-06 (SnO_2) QDs show 71.7% and 79.2% of scavenging activity whereas bare Ag-00 (SnO_2) QDs show 0.39% of scavenging activity as shown in Fig. S8(B).† As bare Ag-00 (SnO_2) QDs show less antioxidant activity we further incubated them for 24 h which showed 3.68% of scavenging activity. In the DPPH radical scavenging test, the enhanced antioxidant activity of Ag-doped SnO_2 QDs is due to their modified surface chemistry. Ag doping creates more surface defects and oxygen vacancies, providing active sites that interact with DPPH radicals. These sites donate electrons or hydrogen atoms to DPPH, reducing it more efficiently. Ag also improves the electron transfer rate, accelerating the scavenging process. Therefore, the improved surface reactivity from Ag doping directly boosts DPPH radical neutralization. A higher number of surface defects and oxygen vacancies generally shows a positive correlation with increased radical scavenging activity.[85] From this analysis, bare Ag-00 (SnO_2) QDs have very little antioxidant activity or are negligible, but after doping with Ag nanoparticles it shows excellent antioxidant activity.[84]

4. Conclusion

In summary, three Ag ions substituted SnO_2 QD samples [$Ag_xSn_{1-x}O_2$ ($x = 0.00$, 0.03 and 0.06)] were fabricated using the wet chemical co-precipitation technique to investigate their performance as photodetectors and also the efficacy in reducing oxidative stress. Additionally, a study on the interactions with *p*-nitrophenol for possible photodegradation application was also conducted. Recorded X-ray diffractograms at room temperature verified the phase-formation without the presence of impurity phases in all the QD samples. Sherrer's formula was used to determine the mean crystallite sizes for each sample and were found in between 2.9 nm to 3.4 nm, which were below of Bohr excitonic diameter confirming the quantum dot nature of the samples. The quantum dot size of the prepared nanomaterials was further confirmed by obtained HRTEM micrographs. Both the phase-purity and local crystallographic symmetry were further verified by analyzing the registered Raman spectra at 300 K. The EDS spectra verified the presence of all three elements (Sn, Ag, and O) in the QD samples. The difference in ionic radii between Ag and Sn ions causes Ag ions to be doped inside the host SnO_2 structure, which results in point defects and changes in the lattice constant. The blue shift was observed in the absorption spectra for higher Ag-content QD samples. The synthesized QDs have excellent absorption properties in the UV band, which makes them useful for a wide range of optical applications. Room temperature FTIR spectra also showed an alteration of characteristic vibrations due to the modifications in the chemical bond lengths caused by Ag doping. Compared to pure SnO_2, Ag-doped SnO_2 QDs showed relatively less photoluminescence (PL) intensity, suggesting improved charge separation and decreased electron–hole recombination. Because of its increased specific surface area, the highest Ag-doped SnO_2 QD samples were found to have more active sites and be more suited for various applications, including photodetector, photocatalytic and antioxidant properties. As evident by Hall coefficients obtained at room temperature, doping of Ag ions turned the pure SnO_2 QDs into n-type semiconductor from p-type. The 6% Ag doped SnO_2 QDs showed comparatively better performance as photodetector. The negative change in Gibbs free energy while studying the interactions between nanocatalysts and *p*-nitrophenol pollutants confirmed the

spontaneous reactions and the interactions were thermodynamically favourable, leading to degrading *p*-nitrophenol into less toxic compounds. Additionally, we examined the capacity of each pure and doped QD sample to scavenge free radicals, and the results showed that SnO_2 QDs doped with Ag ions had antioxidant properties that were noticeably superior to those of pure SnO_2 QDs. On a concluding note, the Ag-doped SnO_2 QDs have shown potential benefits in oxidative stress reduction, photodetector and photodegradation.

Data availability

The raw data has been stored in IASST's D – Space repository.

Author contributions

R. S.: methodology, investigation, formal analysis, discussion, writing original draft, and writing – review and editing, B. B.: investigation, formal analysis, discussion, writing original draft, and writing – review and editing, A. P.: investigation, formal analysis, discussion, writing original draft, and writing – review and editing, M. P. G.: conceptualization, methodology, resources, validation, discussion, writing part of the original draft, writing review and editing, D. C.: conceptualization, methodology, validation, resources, supervision, discussion, and writing review and editing.

Conflicts of interest

The authors declare no competing financial interest.

Acknowledgements

The authors thank the SAIC-IASST for providing instrumental facilities. R. S. thanks UGC, New Delhi for fellowship. B. B. thanks CSIR, New Delhi for fellowship. M. P. G. thanks DST-SERB (ANRF) for fellowship through NPDF (PDF/2023/001314) scheme. All the authors thank IASST, Guwahati for in-house project. RS thanks Dr Samir Thakur for the fruitful discussion. All the authors are grateful of Centre for Nanotechnology, IIT Guwahati for providing the device fabrication facilities.

References

1 G. Yang, J. Li, M. Wu, X. Yu and J. Yu, *Adv. Electron. Mater.*, 2023, **9**, 2300340.
2 B. Ezhilmaran, A. Patra, S. Benny, S. V. Bhat and C. S. Rout, *J. Mater. Chem. C*, 2021, **9**, 6122–6150.
3 T. Shan, X. Hou, X. Yin and X. Guo, *Front. Optoelectron.*, 2022, **15**, 49.
4 Q. Ye, X. Zhang, R. Yao, D. Luo, X. Liu, W. Zou, C. Guo, Z. Xu, H. Ning and J. Peng, *Crystals*, 2021, **11**, 1479.
5 W. J. Lee, S.-S. Lee, S.-H. Sohn, Y. Choi and I.-K. Park, *ACS Photonics*, 2023, **10**, 3901–3914.
6 A. Karabulut, M. Unlu, M. Yıldırım, D. A. Köse, M. O. Erdal and D. E. Yıldız, *J. Mater. Sci. Mater. Electron.*, 2024, **35**, 362.
7 F. P. G. De Arquer, A. Armin, P. Meredith and E. H. Sargent, *Nat. Rev. Mater.*, 2017, **2**, 16100.
8 R. Saran and R. J. Curry, *Nat. Photonics*, 2016, **10**, 81–92.
9 S. R. Mishra and Md. Ahmaruzzaman, *Nanoscale*, 2021, **14**, 1566–1605.
10 Y. Q. Guo, Y. Li, R. Q. Tan and W. J. Song, *Mater. Sci. Eng., B*, 2010, **171**, 20–24.
11 B. Bathula, T. R. Gurugubelli, J. Yoo and K. Yoo, *Catalysts*, 2023, **13**, 765.
12 C. Wang, W. Zeng, L. Luo, P. Zhang and Z. Wang, *Ceram. Int.*, 2016, **42**, 10006–10013.
13 N. Bhardwaj, A. Pandey, B. Satpati, M. Tomar, V. Gupta and S. Mohapatra, *Phys. Chem. Chem. Phys.*, 2016, **18**, 18846–18854.
14 L. K. Sharma, R. K. Choubey and S. Mukherjee, *Mater. Chem. Phys.*, 2020, **254**, 123537.
15 M. S. Inpasalini, A. Singh and S. Mukherjee, *J. Mater. Sci. Mater. Electron.*, 2016, **27**, 4392–4398.
16 M. S. Inpasalini, R. K. Choubey and S. Mukherjee, *J. Electron. Mater.*, 2016, **45**, 3562–3569.
17 S. P. Kim, M. Y. Choi and H. C. Choi, *Mater. Res. Bull.*, 2015, **74**, 85–89.
18 S. Shabna, S. S. J. Dhas and C. S. Biju, *Catal. Commun.*, 2023, **177**, 106642.
19 G. Ramanathan and K. R. Murali, *J. Appl. Electrochem.*, 2022, **52**, 849–859.
20 Y. Kong, Y. Li, X. Cui, L. Su, D. Ma, T. Lai, L. Yao, X. Xiao and Y. Wang, *Nano Mater. Sci.*, 2021, **4**, 339–350.
21 M. Chen, X. Chen, W. Ma, X. Sun, L. Wu, X. Lin, Y. Yang, R. Li, D. Shen, Y. Chen and S. Chen, *ACS Nano*, 2022, **16**, 9631–9639.
22 M. S. Kiani, Z. T. Sadirkhanov, A. G. Kakimov, H. P. Parkhomenko, A. Ng and A. N. Jumabekov, *Nanomaterials*, 2022, **12**, 2615.
23 L. Gao, G. Wu, J. Ma, T. Jiang, B. Chang, Y. Huang and S. Han, *ACS Appl. Mater. Interfaces*, 2020, **12**, 12982–12989.
24 V. K. Vidhu and D. Philip, *Spectrochim. Acta, Part A*, 2014, **134**, 372–379.
25 S. Begum and Md. Ahmaruzzaman, *J. Photochem. Photobiol. B Biol.*, 2018, **184**, 44–53.
26 W. Loh, C. Brinatti and K. C. Tam, *Biochim. Biophys. Acta Gen. Subj.*, 2015, **1860**, 999–1016.
27 L. D. Hansen, G. W. Fellingham and D. J. Russell, *Anal. Biochem.*, 2010, **409**, 220–229.
28 Y. Chen, J. Wang, T. Xu, M. Liu, J. Liu, H. Huang and F. Ouyang, *Curr. Appl. Phys.*, 2020, **20**, 391–399.
29 S. Abbas and J. Kim, *Sensor Actuator Phys.*, 2020, **303**, 111835.
30 S. Yuvaraja, V. Kumar, H. Dhasmana, A. Kumar, A. Verma and V. K. Jain, *J. Mater. Sci. Mater. Electron.*, 2019, **30**, 7618–7628.
31 M. Kumar, A. Saravanan, S. A. Joshi, S.-C. Chen, B.-R. Huang and H. Sun, *Sensor Actuator Phys.*, 2024, **373**, 115441.
32 R. Sonkar, N. J. Mondal, S. Thakur, E. Saikia, M. P. Ghosh and D. Chowdhury, *Nanoscale Adv.*, 2023, **5**, 7042–7056.
33 S. M. Yakout, *J. Mater. Sci. Mater. Electron.*, 2019, **30**, 17053–17065.
34 P. Suriya, M. Prabhu, E. S. Kumar and K. Jagannathan, *Optik*, 2022, **260**, 168971.

35 K. Kumari and Md. Ahmaruzzaman, *Mater. Res. Bull.*, 2023, **168**, 112446.
36 R. Sonkar, N. J. Mondal, B. Boro, M. P. Ghosh and D. Chowdhury, *J. Phys. Chem. Solids*, 2023, **185**, 111715.
37 R. M. Youssef, A. M. S. Salem, A. Shawky, S. Ebrahim, M. Soliman, M. S. A. Abdel-Mottaleb and S. M. El-Sheikh, *J. Materiomics*, 2022, **8**, 1172–1183.
38 S. Thakur, S. M. Borah, A. Singh, D. Saikia and N. C. Adhikary, *J. Electron. Mater.*, 2023, **52**, 4878–4894.
39 S. Podder, J. Bora, S. Thakur, D. Gogoi, B. Basumatary, S. M. Borah, N. C. Adhikary and A. R. Pal, *Mater. Chem. Phys.*, 2021, **275**, 125290.
40 H. Y. Lee and S. N. Yi, *J. Korean Phys. Soc.*, 2023, **82**, 1078–1083.
41 N. J. Mondal, R. Sonkar, S. Thakur, N. Ch. Adhikary and D. Chowdhury, *ACS Appl. Nano Mater.*, 2023, **6**, 7351–7363.
42 R. Sonkar, M. P. Ghosh, S. Thakur, E. Saikia and D. Chowdhury, *Mater. Chem. Phys.*, 2025, **337**, 130578.
43 B. Boro, R. S. Warkhedkar, R. Sonkar and D. Chowdhury, *ChemistrySelect*, 2025, **10**, e202405895.
44 S. Kumar, N. Bhawna, S. K. Yadav, A. Gupta, R. Kumar, J. Ahmed, M. Chaudhary, N. Suhas and V. Kumar, *Environ. Sci. Pollut. Res.*, 2022, **29**, 47448–47461.
45 R. Mahanta, P. Chetri and D. Bora, *Phys. Scr.*, 2023, **98**, 115955.
46 V. K. Tomer and S. Duhan, *Sensor. Actuator. B Chem.*, 2015, **223**, 750–760.
47 N. J. Mondal, R. Sonkar, B. Boro, M. P. Ghosh and D. Chowdhury, *Nanoscale Adv.*, 2023, **5**, 5460–5475.
48 Y. Wang, N. Su, J. Liu, Y. Lin, J. Wang, X. Guo, Y. Zhang, Z. Qin, J. Liu, C. Zhang, X. Qu, W. Li, C. Fu, J. Wang and Q. Zhang, *Results Phys.*, 2022, **37**, 105515.
49 S. Malvankar, S. Doke, R. Gahlaut, E. Martinez-Teran, A. A. El-Gendy, U. Deshpande and S. Mahamuni, *J. Electron. Mater.*, 2019, **49**, 1872–1880.
50 K. N. Yu, Y. Xiong, Y. Liu and C. Xiong, *Phys. Rev. B:Condens. Matter Mater. Phys.*, 1997, **55**, 2666–2671.
51 S. Bhoir, S. D. Gunjal, A. S. Pathan, A. S. Landge, Y. V. Hase, B. M. Palve, D. L. Gapale and S. A. Arote, *Next Mater.*, 2024, **5**, 100272.
52 E. Boyalı, V. Baran, T. Asar, S. Özçelik and M. Kasap, *J. Alloys Compd.*, 2016, **692**, 119–123.
53 H. He, Z. Xie, Q. Li, J. Li and Q. Zhang, *J. Alloys Compd.*, 2017, **714**, 258–262.
54 R. Fu, X. Jiang, Y. Wang, D. Xia, B. Li, J. Ma, H. Xu, A. Shen and Y. Liu, *Nanoscale*, 2023, **15**, 7460–7465.
55 R. Fu, X. Jiang, Y. Wang, B. Li, J. Ma, H. Xu, A. Shen and Y. Liu, *J. Alloys Compd.*, 2024, **978**, 173533.
56 Q. Ye, R. Yao, G. Su, W. Xu, Z. Zhang, C. Luo, T. Qiu, T. Liu, H. Ning and J. Peng, *ACS Appl. Electron. Mater.*, 2023, **5**, 6650–6659.
57 J. Yang, H. Li, J. Yang, B. Sun, Q. Bao, Z. Tang and Z. Ma, *ACS Appl. Electron. Mater.*, 2022, **4**, 4104–4112.
58 K. Akaike, T. Hosokai, Y. Ono, R. Tsuruta and Y. Yamada, *Adv. Mater. Interfaces*, 2023, **10**, 2201800.
59 D. A. Neamen, *Semiconductor Physics and Devices: Basic Principles*, McGraw-Hill, Europe, 2003.
60 A. Pandey, M. S. Patel, D. K. Chaudhary, S. P. Patel, L. S. Pali, A. Garg and L. Kumar, *J. Phys. D Appl. Phys.*, 2021, **54**, 275502.
61 K. C. Kao, in *Elsevier eBooks*, 2004, pp. 327–380.
62 K. Ozel and A. Yildiz, *Semicond. Sci. Technol.*, 2021, **36**, 095001.
63 X. Hou, B. Liu, X. Wang, Z. Wang, Q. Wang, D. Chen and G. Shen, *Nanoscale*, 2013, **5**, 7831.
64 A. Pandey, F. Singh, A. Garg, D. Kanjilal and L. Kumar, *Opt. Mater.*, 2023, **143**, 114180.
65 S. Suman, U. Pandey, N. Pal, P. Swaminathan and B. N. Pal, *ACS Photonics*, 2023, **11**, 93–101.
66 H. M. Mistry, M. P. Deshpande, A. B. Hirpara, N. M. Suchak, S. H. Chaki, S. Pandya, J. Valand and S. V. Bhatt, *Appl. Surf. Sci.*, 2023, **632**, 157583.
67 C.-L. Hsu and Y.-C. Lu, *Nanoscale*, 2012, **4**, 5710.
68 J.-M. Wu and C.-H. Kuo, *Thin Solid Films*, 2009, **517**, 3870–3873.
69 D. Kim, G. Shin, J. Yoon, D. Jang, S.-J. Lee, G. Zi and J. S. Ha, *Nanotechnology*, 2013, **24**, 315502.
70 Y. Chen, C. Zhu, M. Cao and T. Wang, *Nanotechnology*, 2007, **18**, 285502.
71 H. Chen, L. Hu, X. Fang and L. Wu, *Adv. Funct. Mater.*, 2012, **22**, 1229–1235.
72 J. Cai, X. Xu, L. Su, W. Yang, H. Chen, Y. Zhang and X. Fang, *Adv. Opt. Mater.*, 2018, **6**, 1800213.
73 G. Marimuthu, K. Saravanakumar, K. Jeyadheepan, P. M. Razad, M. Jithin, V. R. Sreelakshmi and K. Mahalakshmi, *Superlattices Microstruct.*, 2019, **128**, 181–198.
74 Y. Li, W. Huang, H. Liu, J. Wang, L. Tian and S. Zhang, *J. Nanopart. Res.*, 2018, **20**, 334.
75 D. Mahapatra and D. Basak, *Sensor Actuator Phys.*, 2020, **312**, 112168.
76 Q. Zheng, Y. Zheng, J. Huang and H. Li, *IEEE Sens. J.*, 2021, **21**, 9825–9832.
77 H. K. Hassun, B. H. Hussein, E. M. T. Salman and A. H. Shaban, *Energy Reports*, 2020, **6**, 46–54.
78 A. Dekkiche, M. O. Bellouber, H. Ferhati, K. Dibi and F. Djeffal, *2024 21st International Conference on Electrical Engineering, Computing Science and Automatic Control (CCE), Mexico City*, Mexico, 2024, pp. 1–4.
79 N. Syed, G. O. Bonin, C. K. Nguyen, M. X. Low, J. Meng, A. Zavabeti, B. J. Murdoch, A. S. R. Chesman, S. Wang, P. Punj, K. A. Messalea, S. Walia, J. Bullock, K. B. Crozier, D. E. Gómez and A. Roberts, *ACS Appl. Nano Mater.*, 2024, **7**, 11184–11194.
80 M. Athira, F. S. K. K and S. Angappane, *Semicond. Sci. Technol.*, 2023, **38**, 055014.
81 C.-H. Lin, T.-T. Chen and Y.-F. Chen, *Opt. Express*, 2008, **16**, 16916.
82 J.-p. Colinge and C. A. Colinge, *Physics of Semiconductor Devices*, Springer Science & Business Media, 2007.
83 L. Xu, L. Qin, Y. Huang, Y. Meng, J. Xu, L. Zhao, W. Zhou, Q. Wang, G. Hao and J. Sun, *Sci. China Mater.*, 2024, **67**, 690–697.
84 D. Das, B. C. Nath, P. Phukon, A. Kalita and S. K. Dolui, *Colloids Surf. B Biointerfaces*, 2013, **111**, 556–560.
85 Y. Wang, W. Kong, L. Wang, J. Z. Zhang, Y. Li, X. Liu and Y. Li, *Phys. Chem. Chem. Phys.*, 2018, **21**, 1336–1343.